

Enhanced Thermally Activated Delayed Fluorescence Through Bridge Modification in Sulfone-Based Emitters Employed in Deep Blue Organic Light-Emitting Diodes

Pachaiyappan Rajamalli^{a*}, Dongyang Chen^a, Wenbo Li^b, Ifor D. W. Samuel^b, David B. Cordes^a, Alexandra M. Z. Slawin^a and Eli Zysman-Colman^{a*}

Received 00th January 20xx,
Accepted 00th January 20xx

DOI: 10.1039/x0xx00000x

www.rsc.org/

Two thermally activated delayed fluorescence (TADF) emitters bearing a new dipyrindyl sulfone core as the electron-accepting unit and di-*tert*-butyl carbazoles as electron-donating units are reported. The two emitters, **pDTCz-2DPyS** and **pDTCz-3DPyS**, differ in the regiochemistry of the substitution about the pyridine rings [**pDTCz-2DPyS** = 9,9'-(sulfonylbis(pyridine-6,3-diyl))bis(3,6-di-*tert*-butyl-9H-carbazole); **pDTCz-3DPyS** = 9,9'-(sulfonylbis(pyridine-5,2-diyl))bis(3,6-di-*tert*-butyl-9H-carbazole)]. Both compounds show blue emission in the range of 450–465 nm, which is in line with theoretical calculations. They have very similar singlet-triplet energy (ΔE_{ST}) gaps (ΔE_{ST} = 0.22 eV and 0.21 eV for **pDTCz-3DPyS** and **pDTCz-2DPyS**, respectively). **pDTCz-2DPyS** has a much larger proportion of delayed emission (26.2%) than **pDTCz-3DPyS** (1.2%). The two compounds show comparable photoluminescence quantum yields of 60% in 2,8-bis(diphenylphosphoryl)dibenzo[b,d]thiophene (PPT) doped films. The performance of organic light-emitting diodes (OLEDs) depends on the host used. The maximum external quantum efficiency (EQE) in the PPT host of **pDTCz-3DPyS** is 7.0%, whilst for **pDTCz-2DPyS** it is 12.4%. High performance is obtained for both materials when bis[2-(diphenylphosphino)phenyl] ether oxide (DPEPO) is used as the host, with a maximum EQE of 13.4% for **pDTCz-3DPyS** and 11.4% for **pDTCz-2DPyS**. In addition, **pDTCz-3DPyS** shows pure blue electroluminescence with CIE color coordinates of (0.15, 0.12) compared to **pDTCz-2DPyS** with coordinates of (0.15, 0.19).

Introduction

Organic light-emitting diodes (OLEDs) have come to the fore as the display technology of choice in a growing number of consumer electronics applications, including flat panel large screen televisions, smart phones, and smart watches.¹ The external quantum efficiency (EQE) of the OLED is dictated in part by the internal quantum efficiency (IQE) of the device that is itself a function of the nature of the emitter material. The maximum IQE is typically 25% when the emitter is fluorescent and increases to 100% for heavy metal phosphorescent emitters.² Iridium-based emitters are now used in state-of-the-art green and red OLEDs.³ However, use of noble metals such as iridium or platinum in phosphorescent emitters remains an issue in terms of environmental sustainability due to their inherent toxicity profile and scarcity.⁴ Moreover, although many blue phosphorescent materials have been developed,^{5,1c,6} their device lifetimes are too short and thus are not suitable for

commercial use,⁷ or they are not sufficiently blue in the device with too high a Commission Internationale de l'Éclairage (CIE) γ -ordinate (γ -ordinate >0.25).⁸ Current OLEDs therefore use blue fluorescent compounds and their EQE_{max} so far does not exceed 12%.⁹ As a consequence, around 50% of the power consumed by a mobile OLED display is linked to blue light generation.^{1b} Very recently, OLEDs using metal-free thermally activated delayed fluorescent (TADF) emitters have become popular as viable alternatives to phosphorescent OLEDs.¹⁰ Although a plethora of TADF emitters have been developed since 2012,¹¹ only a few deep-blue TADF OLEDs with CIE coordinates meeting the criteria of $\gamma < 0.2$ and $x + \gamma < 0.30$ are known.^{1b, 12} Moreover, their efficiencies are still lower than sky blue and green TADF OLEDs.

In TADF emitters the lowest triplet excited state (T_1) can be converted to the lowest singlet excited state (S_1) via reverse intersystem crossing (RISC) due to the small singlet-triplet energy gap (ΔE_{ST}) between these two states. The molecular design required to achieve efficient RISC is usually predicated on a highly twisted donor-acceptor structure that has a very small exchange integral between the frontier molecular orbitals involved in these excited states.¹³ However, more twisted molecules lead to greater structural relaxation, thus both broadening and red-shifting the emission spectra.¹⁴ As a result of these undesirable traits, the required CIE coordinates for deep blue emission are frequently not achieved. A design

^a Organic Semiconductor Centre, EaStCHEM School of Chemistry, University of St. Andrews, St. Andrews, Fife, KY16 9ST, United Kingdom.

^b Organic Semiconductor Centre, SUPA School of Physics and Astronomy, University of St Andrews, St Andrews, Fife KY16 9SS, United Kingdom

Electronic Supplementary Information (ESI) available: [General Information, detailed synthesis procedure, emission spectra in various solvents and device performance; CIF of the crystal structure, CCDC 1908262]. See DOI: 10.1039/x0xx00000x

strategy that employs rigid donor-acceptor structures is an attractive solution to achieve efficient, deep blue-emitting TADF-based OLEDs. To address the challenge of deep blue TADF emitters, we designed two compounds based on the scaffold D-het-SO₂-het-D, where D is a donor group that in this case is 3,6-di-*tert*-butyl-9H-carbazole (DTCz) and het is a pyridine ring. The choice of DTCz as the donor resulted from a recognition that the *tert*-butyl groups protected the reactive 3- and 6-positions of the carbazole thereby improving both the chemical and electrochemical stability.¹⁵ The two emitters, **pDTCz-2DPyS** and **pDTCz-3DPyS** (Fig. 1), differ only in the regiochemistry of the substitution about pyridine ring and are both linear structures. The presence/absence of the heteroatom directly influences the performance of these two emitters by facilitating a more planar conformation and is contrasted to the previously reported state-of-the-art deep blue TADF emitter **pDTCz-DPS**.¹⁶ Compound **pDTCz-3DPyS** not only shows deep blue emission and improved device performance (EQE_{max} ~ 13%) compared to **pDTCz-2DPyS**, both OLEDs reported herein show higher EQE_{max} than the reference blue emitter **pDTCz-DPS** using the same device architecture.

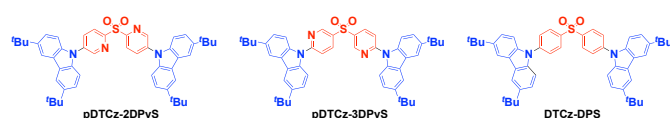
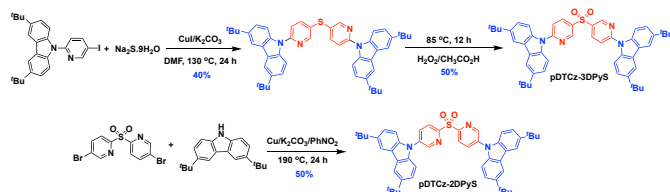


Fig. 1 Emitters in study

Result and discussion

Synthesis

The syntheses of **pDTCz-2DPyS** and **pDTCz-3DPyS** are shown in Scheme 1. The two emitters were purified first by silica gel chromatography and then by temperature gradient vacuum sublimation, and were characterized by a combination of NMR spectroscopy, high-resolution mass spectrometry, melting point determination, elemental analysis, and for **pDTCz-2DPyS** single crystal diffraction analysis (Fig. S1). The purity of the materials was corroborated by high performance liquid chromatography (HPLC) analysis.



Scheme 1. Synthesis of **pDTCz-3DPyS** and **pDTCz-2DPyS**.

Thermal analysis

The thermal stability of these materials was investigated using thermogravimetric analysis (TGA) and differential thermal analysis (DTA). Both **pDTCz-3DPyS** and **pDTCz-2DPyS** showed very high thermal stability with very high melting (T_m) and degradation temperatures (T_d). Melting temperatures of 361 °C

and 353 °C, for **pDTCz-3DPyS** and **pDTCz-2DPyS**, respectively, were observed. The TGA results of these emitters are shown in Fig. 2 and both materials exhibited high decomposition temperature and the T_d (weight loss of 5%) for **pDTCz-3DPyS** and **pDTCz-2DPyS** are 448 °C and 391 °C, respectively. The high thermal stability of these emitters is a desirable feature for the stability of the device morphology stability at high driving voltage and brightness.

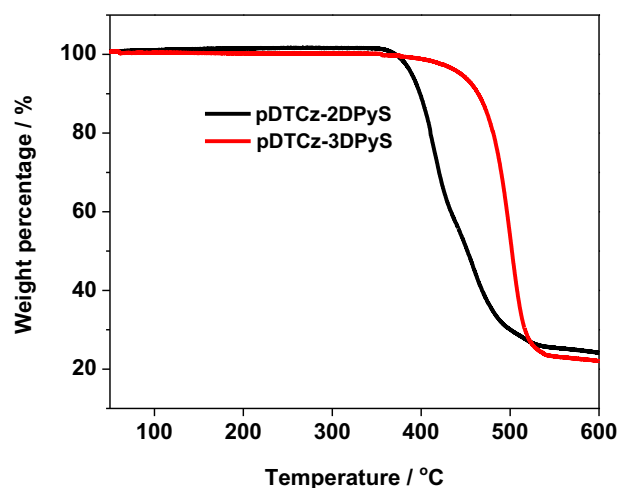


Fig. 2 The thermogravimetric thermograms of **pDTCz-3DPyS** and **pDTCz-2DPyS**.

Density functional theoretical (DFT) calculations

To gain insight into their structure-property relationships, we performed density functional theoretical (DFT) calculations on **pDTCz-2DPyS**, **pDTCz-3DPyS** and the reference emitter **pDTCz-DPS**. Ground state geometry optimization was performed using the PBE0¹⁷ functional with the Pople¹⁸ 6-31G(d,p) basis set while the nature of the excited states was predicted using the Tamm-Dancoff approximation (TDA) to time-dependent density functional theory (TD-DFT).¹⁹ Fig. 3 shows the relative orbital energies and electron density distribution of the HOMO and LUMO of each of the three modelled emitters. In each case, the HOMO is localized on the DTCz donors and slightly extending to the pyridyl/phenyl bridges while the LUMO is localized on both the sulfone and pyridyl/phenyl rings. Among the three molecules, **pDTCz-3DPyS** shows higher oscillator strength ($f = 0.78$) compared to **pDTCz-2DPyS** ($f = 0.35$) and the reference compound **pDTCz-DPS** ($f = 0.48$) (Fig. 3). This is because of more overlap between the HOMO and LUMO, and the value is very high compared with other TADF molecules. Both **pDTCz-2DPyS** and **pDTCz-3DPyS** show comparable calculated ΔE_{ST} and S_1 and T_1 energies (Table 1). The high S_1 energy of these molecules and the small calculated ΔE_{ST} values are indications that these materials are deep blue TADF emitters.

Table 1. Calculated HOMO/LUMO and $S_1/T_1/\Delta E_{ST}$ energies for **pDTCz-2DPyS**, **pDTCz-3DPyS** and **pDTCz-DPS**.

Compound	HOMO / eV	LUMO / eV	S_1 / eV	T_1 / eV	ΔE_{ST} / eV	f
pDTCz-3DPyS	-5.77	-1.71	3.45	3.02	0.43	0.78
pDTCz-2DPyS	-5.74	-1.51	3.51	3.12	0.39	0.35
pDTCz-DPS	-5.63	-1.50	3.48	3.13	0.35	0.48

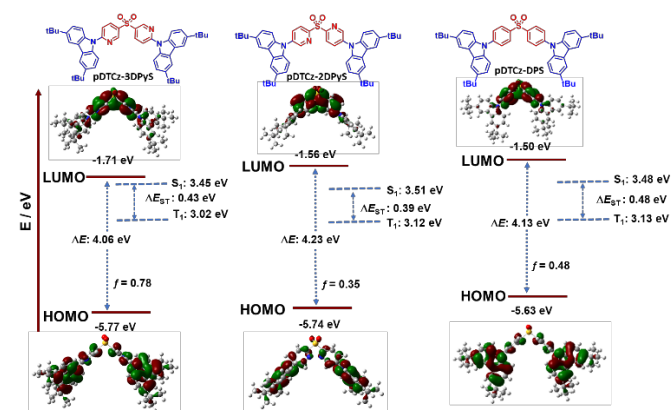


Fig. 3 Calculated HOMO, LUMO, S_1 and T_1 energies, and electron-density distributions of the HOMO and LUMO of **pDTCz-2DPyS**, **pDTCz-3DPyS** and **pDTCz-DPS**.

Optoelectronic Characterization

Electrochemical measurements on **pDTCz-2DPyS**, and **pDTCz-3DPyS** were carried out in DCM. The cyclic voltammetry (CV) traces are shown in Fig. 4. The DTCz-centered oxidation waves were found to be reversible while the dipyrindylsulfone-based reduction waves were found to be irreversible. The oxidation potentials for **pDTCz-2DPyS** ($E_{1/2}^{ox} = 1.29$ V) and **pDTCz-3DPyS** ($E_{1/2}^{ox} = 1.25$ V) are, expectedly, closely aligned. The small cathodic shift in the latter reflects the increased planarized conformation of the DTCz groups and their resulting increased conjugation with the 3DPyS acceptor core. The corresponding HOMO levels of -5.75 eV and -5.71 eV for **pDTCz-2DPyS** and **pDTCz-3DPyS**, respectively, closely match those predicted by DFT calculations (-5.74 eV for **pDTCz-2DPyS** and -5.77 eV for **pDTCz-3DPyS**). The reduction potentials for **pDTCz-2DPyS** ($E^{red} = -1.99$ V) and **pDTCz-3DPyS** ($E^{red} = -2.06$ V) are likewise closely aligned. The LUMO levels of -3.15 eV and -3.08 eV for **pDTCz-2DPyS** and **pDTCz-3DPyS**, respectively, were obtained directly from the reduction potentials. More destabilized LUMO levels of -2.73 eV and -2.57 eV, respectively for **pDTCz-2DPyS**, and **pDTCz-3DPyS** were estimated by adding E_g to the HOMO (Table 2), where the E_g is the singlet energy gap and determined from the onset of the fluorescence spectrum, which was measured in thin film (vide infra); these are more in line with the DFT calculated values.

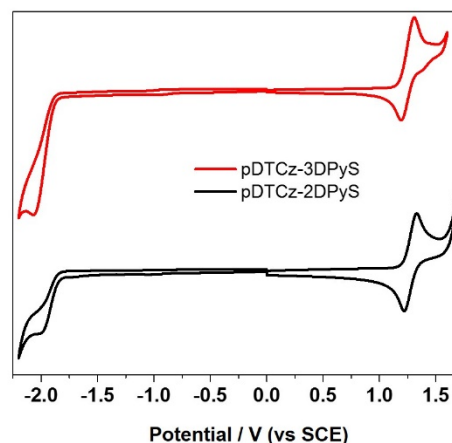


Fig. 4 Cyclic Voltammograms of **pDTCz-2DPyS** and **pDTCz-3DPyS** in DCM, reported versus SCE ($Fc/Fc^+ = 0.34$ V in DCM)²⁰ and scan rate = 50 mV/s.

The UV-vis absorption and steady-state photoluminescence (PL) spectra of **pDTCz-2DPyS** and **pDTCz-3DPyS** in toluene are shown in Fig. 5. Both compounds show an intramolecular charge transfer (ICT) absorption band at 356 nm and 367 nm, respectively, for **pDTCz-2DPyS** and **pDTCz-3DPyS**. The larger molar absorptivity, ϵ , and bathochromic shift of the ICT band in the latter are consistent with the picture produced by the DFT modelling (Fig. 3). However, the photoluminescence spectra in toluene are identical for both emitters (Fig. 5a). Indeed, the emission spectra are broad and structureless in solution, and the emission spectra are bathochromically shifted in polar solvents, both indications of an emission from an ICT state (Fig. S2). The Φ_{PL} measured in toluene under an N_2 atmosphere are 47% and 50% for **pDTCz-2DPyS** and **pDTCz-3DPyS**, respectively. When measured under air, these are reduced to 37% and 43%, respectively.

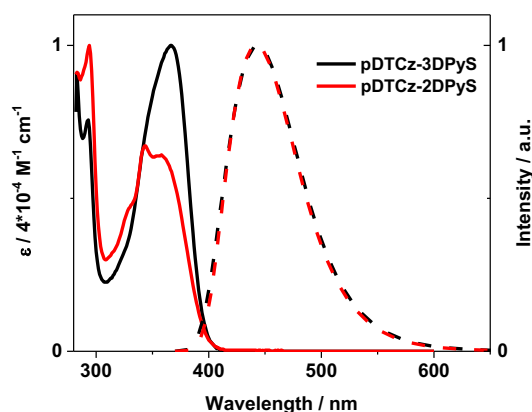


Fig. 5 Absorption (solid) and emission (dashed) spectra of **pDTCz-2DPyS** and **pDTCz-3DPyS** in toluene solution. $\lambda_{exc} = 360$ nm

To assess the emission properties of these emitters in the solid state, their photophysical properties were first investigated in PMMA. Thin films were prepared by spin-coating a 10 wt% chlorobenzene solution of emitter in PMMA (Fig. 6a).

All emission maxima are red-shifted slightly, by 5 nm for **pDTCz-3DPyS** and 10 nm for **pDTCz-2DPyS**, and the emission spectra are slightly sharper than those in toluene. The Φ_{PL} in 10 wt% doped PMMA films under an N_2 atmosphere are 51% and 52%, respectively for **pDTCz-2DPyS** and **pDTCz-3DPyS**. The Φ_{PL} values were reduced to 44% and 47%, respectively, under air, indicating the presence of an accessible triplet state in both solution and thin film state.

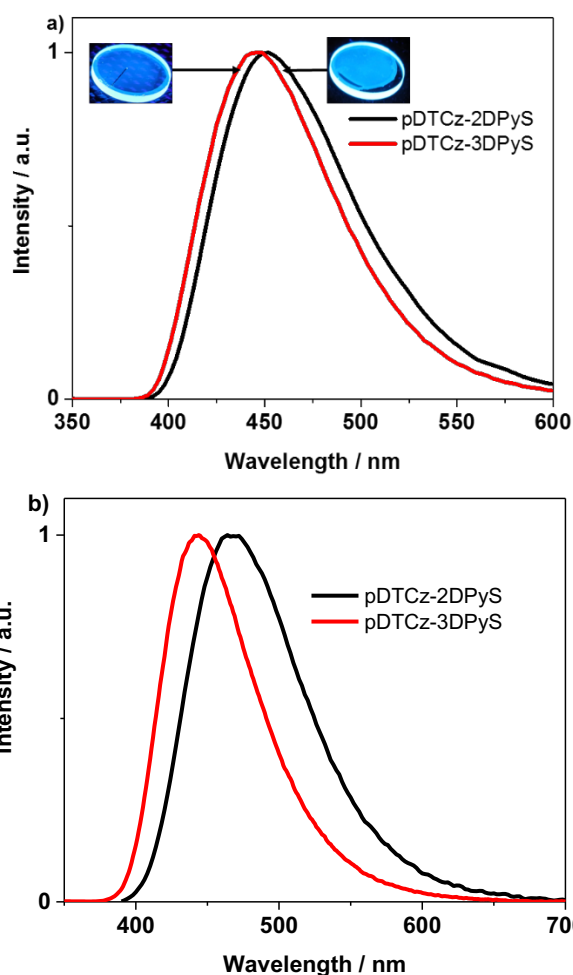


Fig. 6 Emission spectra of **pDTCz-2DPyS** and **pDTCz-3DPyS** in a) 10 wt% doped PMMA film and, b) 7 wt% doped PPT film. $\lambda_{\text{exc}} = 360$ nm.

Given their high excited state energies in toluene and in PMMA, the photophysical properties in doped thin films in a suitably high triplet energy host, PPT, were next investigated. The room temperature steady-state emission spectra, shown in Fig. 6b, remain featureless. The Φ_{PL} measured in 7 wt% doped PPT film under an N_2 atmosphere are higher still at 67%, 62%, and 60%, respectively, for **pDTCz-2DPyS**, **pDTCz-3DPyS** and **pDTCz-DPS**. The Φ_{PL} values decreased to 55%, 49% and 59%, respectively, under air. The small decrease of PLQY on going from nitrogen to air suggests that only a relatively small part of the emission is from delayed fluorescence. In order to elucidate ΔE_{ST} the fluorescence and phosphorescence spectra were measured at 300 K and 77 K, respectively (Fig. 7 and Fig. S3 and

S4) and the ΔE_{ST} , calculated from the difference between the onsets of these spectra, were found to be 0.21 and 0.22 eV for **pDTCz-2DPyS** and **pDTCz-3DPyS**, respectively. These values are slightly lower than the calculated values though follow the same trend (Table 1). They are also lower than **pDTCz-DPS** ($\Delta E_{\text{ST}} = 0.27$ eV) and denote an efficient rISC mechanism in both PPT and DPEPO (*vide infra*). The photophysical data are summarized in Table 2. Here, **pDTCz-3DPyS** has a larger ΔE_{ST} compared to the **pDTCz-2DPyS**, which we attribute to the more planarized conformation in the former (DFT calculated angle between the plane of the TCz and the plane of the pyridine = 33.2° for **pDTCz-3DPyS** and 48.1° for **pDTCz-2DPyS**).

The time-resolved photoluminescence (PL) was measured in a toluene solution of concentration 10^{-5} M and the results are shown in Fig. 8a. **pDTCz-3DPyS** shows a biexponential decay with prompt, τ_{p} , and delayed, τ_{d} , fluorescence lifetimes of 7.1 ns (95.4%) and 0.45 μs (4.6%), respectively.

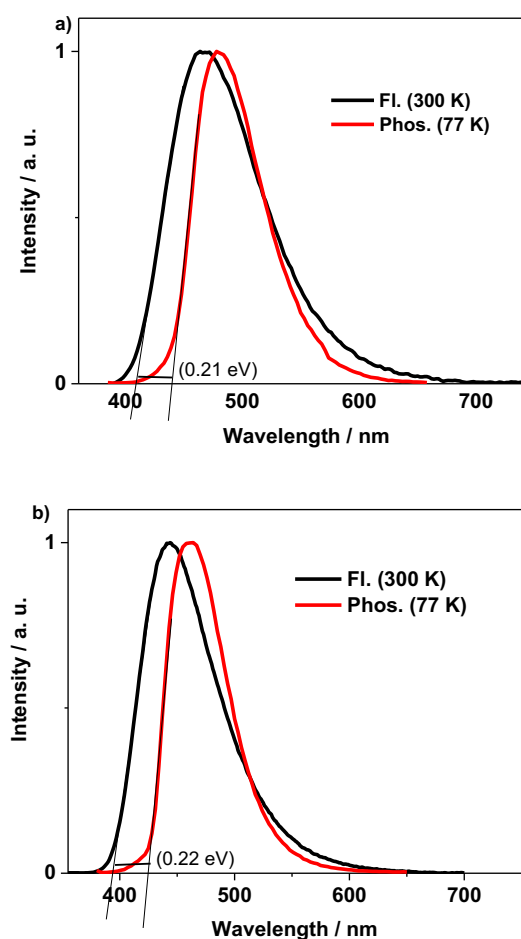


Fig. 7 Fluorescence (Fl.) phosphorescence (Phos.) spectra and of a) **pDTCz-2DPyS**, and b) **pDTCz-3DPyS** in 7 wt% doped PPT film. $\lambda_{\text{exc}} = 360$ nm

pDTCz-2DPyS also shows biexponential decay with τ_{p} and τ_{d} of 15.1 ns (84.1%) and 0.85 μs (15.9%), respectively. The results support that these materials emit by TADF in toluene solution. The time-resolved PL profiles in doped PPT films are shown in Fig. 8b. Similar to the measurements in PhMe, in both compounds there is a dominant prompt nanosecond

component and a delayed microsecond component that is itself two orders of magnitude longer than that observed in solution. For **pDTCz-3DPyS** the τ_p is 7.0 ns (98.8%) and the τ_d is 33.2 μ s (1.2%) while for **pDTCz-2DPyS** the τ_p is 13.3 ns (73.8%) and the τ_d is biexponential in nature with 27.1 μ s (16.4%) and 99.5 μ s (9.8%). We next performed variable temperature time-resolved PL measurements to corroborate

the TADF nature of the emission. As shown in Fig. 9, **S3** and **S4**, the relative intensities of the delayed PL of both **pDTCz-2DPyS** and **pDTCz-3DPyS** decreased from 300 to 77 K in both PPT and DPEPO host and phosphorescence emission is increased at 77 K.²¹

Table 2. Photophysical properties of **pDTCz-3DPyS** and **pDTCz-2DPyS**.

Emitter	λ_{abs} / nm ^a	λ_{PL} / nm ^b	λ_{PL} / nm ^c	HOMO / eV ^d	LUMO / eV ^e	$E_g(S_1)$ / eV ^f	$E_T(T_1)$ / eV ^g	ΔE_{ST} / eV ^h	Φ_{PL} / % ⁱ
pDTCz-3DPyS	367	444	462	-5.71	-2.57	3.14	2.92	0.22	62
pDTCz-2DPyS	356	467	478	-5.75	-2.73	3.02	2.81	0.21	67

^a ICT band measured in PhMe at room temperature. ^b Fluorescence spectra measured in co-doped film at 300 K in PPT host. ^c Phosphorescence spectra measured in a film with 7 wt% in PPT host at 77 K. ^d Determined from the oxidation potential observed by CV in 10⁻³ M DCM. ^e Calculated from HOMO + E_g . ^f E_g values are estimated from the onset of the fluorescence spectrum. ^g Estimated from the onset of phosphorescence spectrum. ^h $\Delta E_{\text{ST}} = E(S_1) - E(T_1)$. ⁱ Absolute Φ_{PL} of 7 wt% PPT film measured using an integrating sphere.

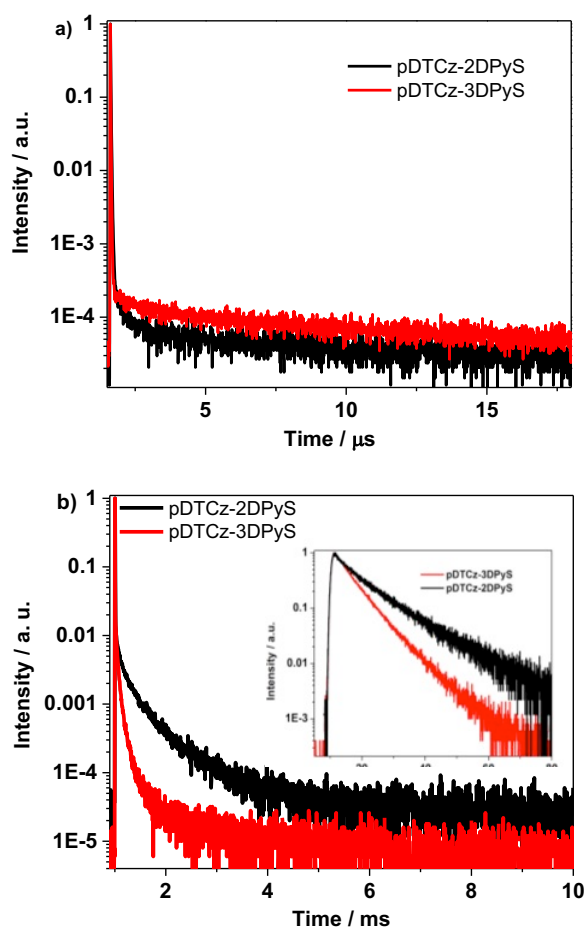


Fig. 8 a) Time-resolved (TCSPC) PL of emitter in toluene solution, and b) Time-resolved (MCS) PL of 7 wt% emitter doped in PPT thin film at 300 K (Inset: prompt emission measured by TCSPC of PPT doped film). $\lambda_{\text{exc}} = 378$ nm.

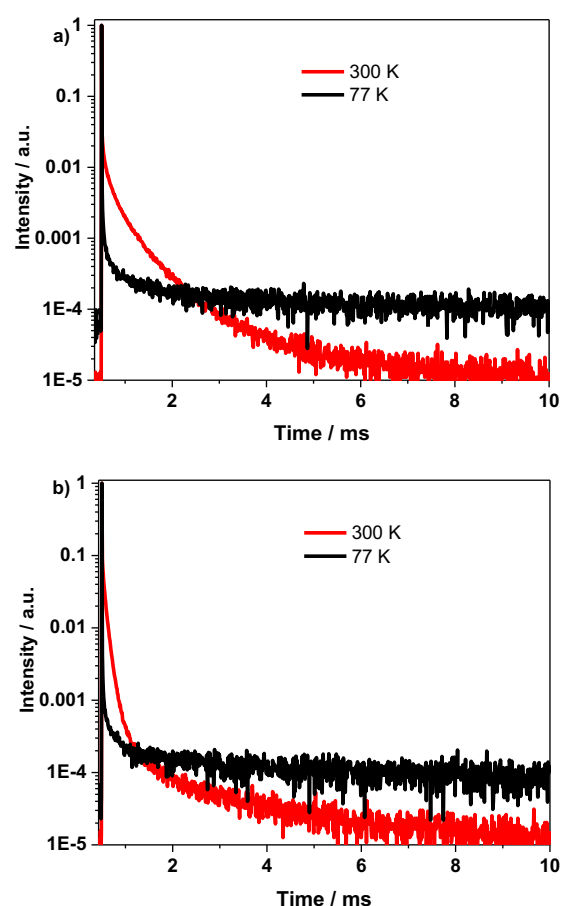


Fig. 9 Variable temperature time-resolved PL of 7 wt% doped thin films in PPT of a) **pDTCz-2DPyS**, and b) **pDTCz-3DPyS**. $\lambda_{\text{exc}} = 378$ nm

Device performance

Given their promising photophysical properties, we next fabricated multilayer devices using these dopants. The schematic representation of the device architecture and

molecular structures of the materials used in the devices are shown in Fig. 10.

Table 3. The electroluminescence performances of the OLEDs using pDTCz-3DPyS, pDTCz-2DPyS and pDTCz-DPS.^{a,b}

Device (Emitter)	L_{\max} / cd m ⁻²	EQE_{\max} ; EQE_{100} / %	CE_{\max} ; CE_{100} / cd/A	PE_{\max} ; PE_{100} / lm/W	λ_{EL} / nm	CIE @6 V
Device A (pDTCz-3DPyS)	2530	7.0;5.7	6.5;5.2	5.9;3.1	453	(0.15, 0.12)
Device B (pDTCz-2DPyS)	3850	12.4;7.7	17.1;10.4	15.3;6.0	467	(0.15, 0.19)
Device C (pDTCz-DPS)	1790	2.7;2.6	1.4;1.3	1.1;1.0	428	(0.15, 0.08)

^a Configuration for Devices A, B and C: ITO/NPB (30 nm)/TAPC (20 nm)/mCP (10 nm)/PPT: pDTCz-3DPyS or pDTCz-2DPyS or pDTCz-DPS (7 wt%) (30 nm)/PPT (5 nm)/TmPyPb (30 nm)/LiF (1 nm)/Al (100 nm); ^b V_0 , The operating voltage at a brightness of 1 cd m⁻²; L, luminance; EQE, external quantum efficiency; CE, current efficiency; PE, power efficiency; Data are reported as maxima and at 100 cd m⁻²; and λ_{EL} , the wavelength where the EL spectrum has the highest intensity.

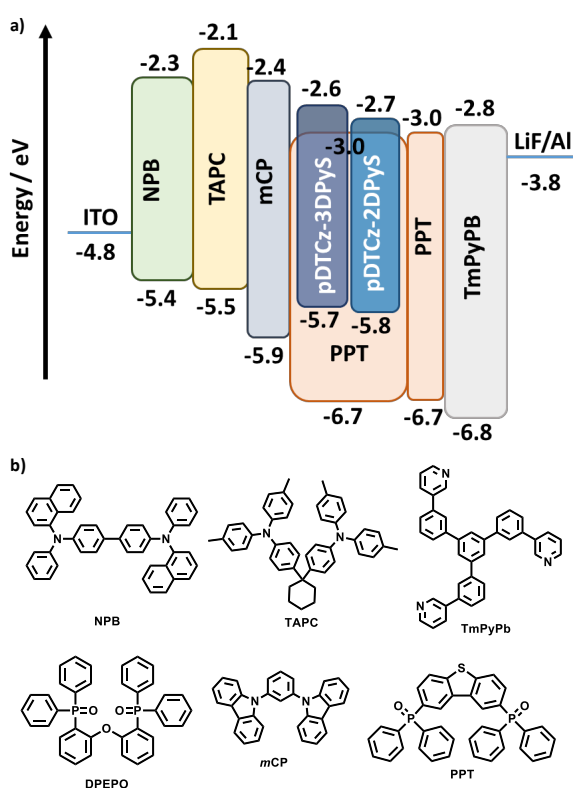


Fig. 10. Schematic representation of the Devices A-C (a) and chemical structures of the materials used in the devices (b).

Devices A, B and C employed, respectively, pDTCz-3DPyS, pDTCz-2DPyS and pDTCz-DPS as the dopant and were fabricated using the following device stack: ITO/NPB (30 nm)/TAPC (20 nm)/mCP (10 nm)/ PPT:Dopant (7 wt%) (30 nm)/ PPT (5 nm)/TmPyPb (30 nm)/LiF (1 nm)/Al (100 nm), respectively. In these devices, *N,N'*-bis(1-naphthyl)-*N,N'*-diphenyl-1,1'-biphenyl-4,4'-diamine (NPB) acts as the hole injection material, 1,1-bis[4-*N,N'*-di(*p*-tolyl)amino]phenyl] cyclohexane (TAPC) is the hole transporting material, 1,3-bis(*N*-carbazolyl)benzene (*m*CP) is the an exciton blocking layer, PPT is the host material, and 2,2',2''-(1,3,5-benzenetriyl)-tris(1-phenyl-1-*H*-benzimidazole) (TmPyPb) is the electron-

transporting material. The electroluminescence properties of the devices are shown in Fig. 11, and Fig. S5, S6, and data are summarized in Table 3.

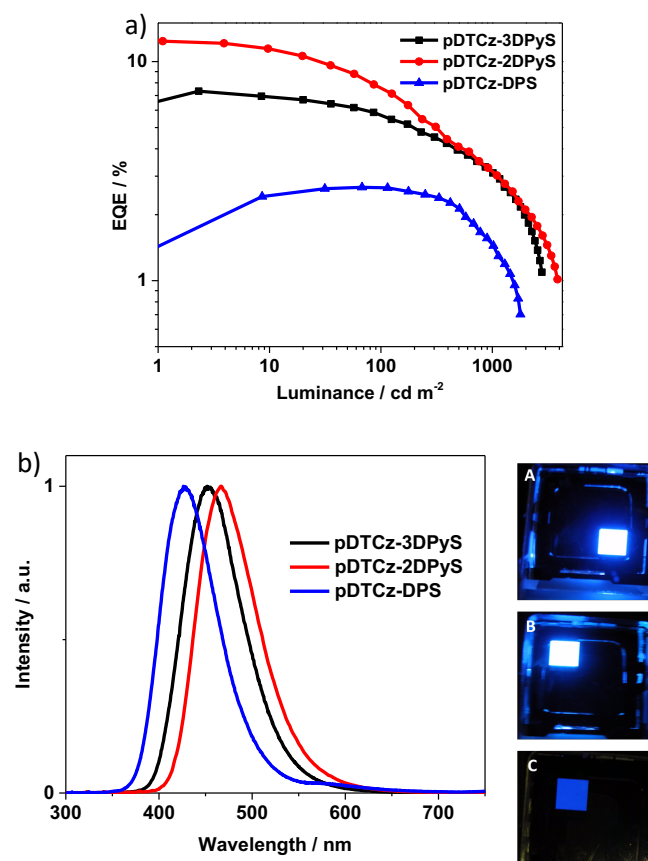


Fig. 11 Electroluminescent performance of Devices A (pDTCz-3DPyS), B (pDTCz-2DPyS) and C (pDTCz-DPS): a) EQE vs luminance, b) Electroluminescence spectra and device photos

Devices A, B and C show maximum external quantum efficiencies (EQE_{\max}) of 7.0%, 12.4%, and 2.7%, respectively. The CIE coordinates of Devices A and B are (0.15, 0.12) and (0.15, 0.19), respectively. Both Devices A and B show an improved performance compared to Device C with the reference emitter pDTCz-DPS. The device performance of these materials are

significantly improved compared to our recently reported oxadiazole-based blue OLEDs ($\text{EQE}_{\text{max}} = 4.7\%$; $\text{CIE}_{x,y} = 0.15, 0.12$).²² Devices A, B and C show maximum current and power efficiencies of 6.5, 17.1, 1.4 cd A^{-1} , and 5.9, 15.3, 1.1 lm W^{-1} , respectively. The use of **pDTCz-2DPyS** as the dopant resulted in a ca. 4.6 times improvement in the EQE_{max} of devices compared with **pDTCz-DPS**. The higher EQE_{max} of Device B is due in part to more efficient singlet harvesting as a function of the smaller ΔE_{ST} .

The electroluminescence spectra of both the devices are very similar to the corresponding PPT thin film PL spectra, with

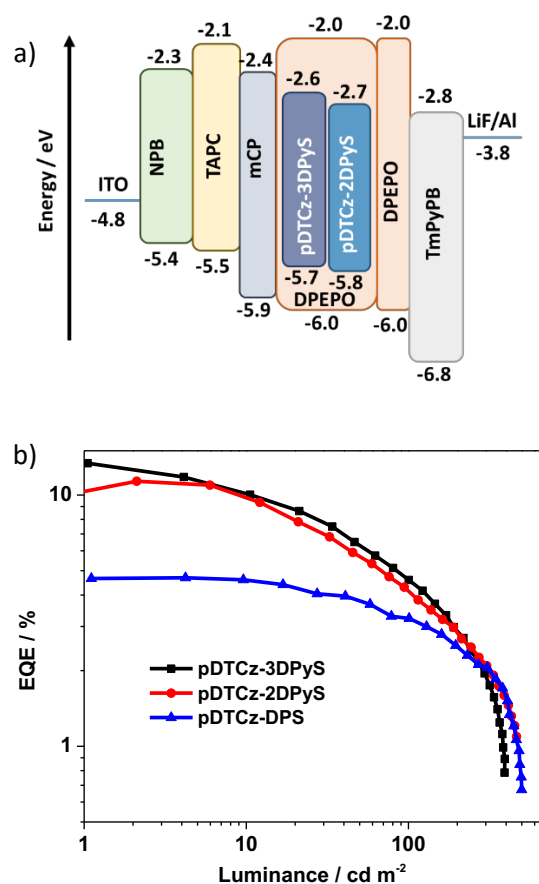
no residual emission exhibited from other layers (Fig. 11). This observation indicates that the excitons are confined within the emission layer. Devices A and B gave blue electroluminescence with λ_{EL} of 453 nm and 467 nm and colour coordinates of (0.15, 0.12) and (0.15, 0.19), respectively, that are red-shifted compared to that of Device C (0.15, 0.08).

Table 4. The electroluminescence performances of the OLEDs using **pDTCz-3DPyS**, **pDTCz-2DPyS** and **pDTCz-DPS**.^{a,b}

Devices	$L_{\text{max}} / \text{cd m}^{-2}$	$\text{EQE}_{\text{max}}; \text{EQE}_{100} / \%$	$\text{CE}_{\text{max}}; \text{CE}_{100} (\text{cd/A})$	$\text{PE}_{\text{max}} / \text{PE}_{100} (\text{lm/W})$	$\lambda_{\text{EL}} / \text{nm}$	CIE @ 6 V
Device D (pDTCz-3DPyS)	392	13.4;4.5	13.2/4.3	10.9/2.3	452	(0.15, 0.13)
Device E (pDTCz-2DPyS)	462	11.4;4.2	15.1/5.8	11.6/2.6	466	(0.15, 0.18)
Device F (pDTCz-DPS)	499	4.6;3.2	2.5/1.7	2.2/1.0	428	(0.15, 0.08)

^a Configuration for Devices D, E and F: ITO/NPB (30 nm)/TAPC (20 nm)/mCP (10 nm)/DPEPO: **pDTCz-3DPyS** or **pDTCz-2DPyS** or **pDTCz-DPS** (7 wt%) (30 nm)/PPT (5 nm)/TmPyPb (30 nm)/LiF (1 nm)/Al (100 nm); ^b V_{d} , The operating voltage at a brightness of 1 cd m^{-2} ; L, luminance; EQE, external quantum efficiency; CE, current efficiency; PE, power efficiency; Data are reported as maxima and at 100 cd m^{-2} ; and λ_{EL} , the wavelength where the EL spectrum has the highest intensity.

A high triplet energy (>3.0 eV) host material with appropriate HOMO and LUMO energy levels is important to achieve high performance deep blue OLEDs. Although, both DPEPO and PPT have the same triplet energy (3.0 eV). The HOMO (6.0 eV) and LUMO (2.0 eV) levels of DPEPO²³ better matched to the HOMO and LUMO of the emitters (Table 3) than when PPT (HOMO 6.7 eV and LUMO 3.0 eV)²⁴ is used as a host (Fig. 10a and Fig.12a). The Φ_{PL} of these emitters, measured under a N_2 atmosphere in 7 wt% DPEPO film, are 81%, 72%, 66%, respectively for **pDTCz-2DPyS**, **pDTCz-3DPyS** and **pDTCz-DPS** and it reduced to 62%, 61% and 59% under air. Therefore, we next checked the device performances in the DPEPO host, Devices D-F were fabricated with same device architecture as Devices A-C but with DPEPO as the host instead of PPT. Devices D, E and F showed maximum EQE_{max} of 13.4%, 11.4%, and 4.7%, respectively (Fig. 12); relevant device metrics are summarized in Table 4. Similar to the results with PPT as the host, Devices D and E show improved performance compared to the reference Device F ($\text{EQE}_{\text{max}} = 4.7\%$). Noticeably, the performance of Device D increased almost twofold ($\text{EQE}_{\text{max}} = 13.4\%$) compared to Device A ($\text{EQE}_{\text{max}} = 7.0\%$). The current and power efficiencies are 13.2, 15.1, 2.5 cd A^{-1} , and 10.9, 11.6, 2.2 lm W^{-1} , respectively, for Devices D, E and F. Devices D and E show a higher EQE_{max} in DPEPO host, but at the expense of lower luminance [392 cd/m^2 (D), 462 cd/m^2 (E) and 499 cd/m^2 (F)] as compared to the devices using PPT as the host [2531 cd/m^2 (D), 3850 cd/m^2 (E) and 1788 cd/m^2 (F)]. We ascribe the lower luminances to poorer charge transport in DPEPO compared to PPT. These results indicate that the performances of the OLEDs can be improved further by selecting high triplet energy ambipolar host materials.



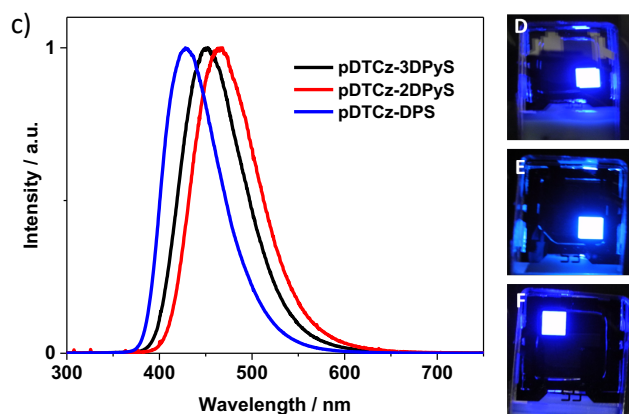


Fig. 12 Electroluminescent performance of Devices D (pDTCz-DPyS), E (pDTCz-DPyS) and F (pDTCz-DPS): a) EQE vs luminance, b) Electroluminescence spectra and device photos.

Conclusions

We have designed two D-A-D TADF emitters **pDTCz-3DPyS** and **pDTCz-2DPyS** bearing pyridyl sulfone electron-accepting units and di-*tert*-butylcarbazoles as the electron-donating units. The experimental ΔE_{ST} values of 0.22 eV and 0.21 eV, respectively, for **pDTCz-3DPyS** and **pDTCz-2DPyS**, the oxygen sensitivity of Φ_{PL} and the temperature-dependent behaviour all point to a TADF-based emission both in solution and in the solid state. Both emitters show attractively high thin film photoluminescence quantum yields of 62–81% in both DPEPO and PPT host. Vacuum-deposited OLEDs showed EQE_{max} of 13.4% and 12.4%, respectively, for the devices with **pDTCz-3DPyS** and **pDTCz-2DPyS**. The performance of the OLEDs with these two emitters is much higher than the device with the reference state-of-the-art deep blue TADF emitter, **pDTCz-DPS** ($EQE \sim 4.7\%$). Importantly, the device with **pDTCz-3DPyS** shows pure blue electroluminescence with CIE coordinates of (0.15, 0.12), while the device employing **pDTCz-2DPyS** shows CIE coordinates of (0.15, 0.19). It suggests that small changes in the structure of the acceptor unit play a crucial role in retaining the pure blue emission and improving the performances of devices. Moreover, the OLED with **pDTCz-3DPyS** as the emitter shows a much higher EQE_{max} of 13.4% in DPEPO host compared to the device with PPT as the host (7.0%) and it implies that selection of the host materials remains very important to achieve highly efficient devices.

Conflicts of interest

There are no conflicts to declare

Acknowledgements

We are grateful to the Engineering and Physical Sciences Research Council (EPSRC) for support from grants EP/P010482/1 and EP/R035164/1. P. Rajamalli acknowledges support from a Marie Skłodowska-Curie Individual Fellowship (MCIF; No. 749557). Dongyang Chen and Wenbo Li thank the

China Scholarship Council (grant numbers 201603780001 and 201708060003).

Notes and references

- (1). (a) S. Reineke, *Nat Mater*, 2015, **14**, 459–462; (b) X. Cai and S.-J. Su, *Adv. Funct. Mater.*, 2018, **28**; (c) Y. Im, S. Y. Byun, J. H. Kim, D. R. Lee, C. S. Oh, K. S. Yook and J. Y. Lee, *Adv. Funct. Mater.*, 2017, **27**; (d) K. T. Kamtekar, A. P. Monkman and M. R. Bryce, *Adv. Mater.*, 2010, **22**, 572–582; (e) R. K. Konidena and J. Y. Lee, *Chem Rec*, 2018.
- (2). (a) M. A. Baldo, D. F. O'Brien, Y. You, A. Shoustikov, S. Sibley, M. E. Thompson and S. R. Forrest, *Nature*, 1998, **395**, 151–154; (b) C. Adachi, M. A. Baldo, M. E. Thompson and S. R. Forrest, *J. Appl. Phys.*, 2001, **90**, 5048–5051.
- (3). (a) D. Ma, T. Tsuboi, Y. Qiu and L. Duan, *Adv Mater*, 2017, **29**, 1603253; (b) T. Tsuboi and W. Huang, *Isr. J. Chem.*, 2014, **54**, 885–896; (c) H. Xu, R. Chen, Q. Sun, W. Lai, Q. Su, W. Huang and X. Liu, *Chem. Soc. Rev.*, 2014, **43**, 3259–3302; (d) F. Xu, H. U. Kim, J.-H. Kim, B. J. Jung, A. C. Grimsdale and D.-H. Hwang, *Prog. Polym. Sci.*, 2015, **47**, 92–121.
- (4). P. Nuss and M. J. Eckelman, *PLoS One*, 2014, **9**, e101298.
- (5). X. Yang, X. Xu and G. Zhou, *J. Mater. Chem. C*, 2015, **3**, 913–944.
- (6). (a) K. S. Yook and J. Y. Lee, *Adv Mater*, 2012, **24**, 3169–3190; (b) K. O. Kirlikovali and A. M. Spokoyny, *Chem*, 2017, **3**, 385–387; (c) L. Xiaoyue, Z. Juanye, Z. Zifeng, W. Liding, Y. Hannan, C. Qiaowen, J. Nan, L. Zhiwei, B. Zuqiang, L. Weiping, L. Zhenghong and H. Chunhui, *Adv. Mater.*, 2018, **30**, 1705005; (d) A. K. Pal, S. Krotkus, M. Fontani, C. F. R. Mackenzie, D. B. Cordes, A. M. Z. Slawin, I. D. W. Samuel and E. Zysman-Colman, *Adv Mater*, 2018, **30**, e1804231.
- (7). D. Jacquemin and D. Escudero, *Chem Sci*, 2017, **8**, 7844–7850.
- (8). (a) Y. Zhang, J. Lee and S. R. Forrest, *Nat Commun*, 2014, **5**, 5008; (b) N. C. Giebink, B. W. D'Andrade, M. S. Weaver, J. J. Brown and S. R. Forrest, *J. Appl. Phys.*, 2009, **105**.
- (9). Y. H. Chen, C. C. Lin, M. J. Huang, K. Hung, Y. C. Wu, W. C. Lin, R. W. Chen-Cheng, H. W. Lin and C. H. Cheng, *Chem Sci*, 2016, **7**, 4044–4051.
- (10). (a) M. Y. Wong and E. Zysman-Colman, *Adv. Mater.*, 2017, **In Press**; (b) Y. Liu, C. Li, Z. Ren, S. Yan and M. R. Bryce, *Nat. Rev. Mater.*, 2018, **3**.
- (11). H. Uoyama, K. Goushi, K. Shizu, H. Nomura and C. Adachi, *Nature*, 2012, **492**, 234–238.
- (12). (a) Y. Li, J.-Y. Liu, Y.-D. Zhao and Y.-C. Cao, *Mater. Today*, 2017, **20**, 258–266; (b) T. T. Bui, F. Goubard, M. Ibrahim-Ouali, D. Gigmes and F. Dumur, *Beilstein J Org Chem*, 2018, **14**, 282–308.
- (13). A. Endo, K. Sato, K. Yoshimura, T. Kai, A. Kawada, H. Miyazaki and C. Adachi, *Appl. Phys. Lett.*, 2011, **98**, 083302.
- (14). (a) Y. J. Cho, S. K. Jeon, S.-S. Lee, E. Yu and J. Y. Lee, *Chem. Mater.*, 2016, **28**, 5400–5405; (b) Y. Im, M. Kim, Y. J. Cho, J.-A. Seo, K. S. Yook and J. Y. Lee, *Chem. Mater.*, 2017, **29**, 1946–1963.
- (15). (a) P. Rajamalli, N. Senthilkumar, P. Gandeepan, P. Y. Huang, M. J. Huang, C. Z. Ren-Wu, C. Y. Yang, M. J. Chiu, L. K. Chu, H. W. Lin and C. H. Cheng, *J Am Chem Soc*, 2016, **138**, 628–634; (b) N. Lin, J. Qiao, L. Duan, H. Li, L. Wang and Y. Qiu, *J. Phys. Chem. C*, 2012, **116**, 19451–19457.
- (16). Q. Zhang, J. Li, K. Shizu, S. Huang, S. Hirata, H. Miyazaki and C. Adachi, *J Am Chem Soc*, 2012, **134**, 14706–14709.
- (17). C. Adamo and V. Barone, *J. Chem. Phys.*, 1999, **110**, 6158–6170.
- (18). J. A. Pople, J. S. Binkley and R. Seeger, *Int. J. Quant. Chem. Symp.*, 1976, **10**, 1.

- (19). M. Moral, L. Muccioli, W. J. Son, Y. Olivier and J. C. Sancho-García, *J. Chem. Theory Comput.*, 2015, **11**, 168-177.
- (20). N. G. Connelly and W. E. Geiger, *Chem. Rev.*, 1996, **96**, 877-910.
- (21). (a) M. Mamada, K. Inada, T. Komino, W. J. Potscavage, Jr., H. Nakanotani and C. Adachi, *ACS Cent Sci*, 2017, **3**, 769-777; (b) S. Gan, S. Hu, X. L. Li, J. Zeng, D. Zhang, T. Huang, W. Luo, Z. Zhao, L. Duan, S. J. Su and B. Z. Tang, *ACS Appl Mater Interfaces*, 2018, **10**, 17327-17334.
- (22). M. Y. Wong, S. Krotkus, G. Copley, W. Li, C. Murawski, D. Hall, G. J. Hedley, M. Jaricot, D. B. Cordes, A. M. Z. Slawin, Y. Olivier, D. Beljonne, L. Muccioli, M. Moral, J. C. Sancho-García, M. C. Gather, I. D. W. Samuel and E. Zysman-Colman, *ACS Appl. Mater. Interfaces*, 2018, **10**, 33360-33372.
- (23). Q. Zhang, T. Komino, S. Huang, S. Matsunami, K. Goushi and C. Adachi, *Adv. Funct. Mater.*, 2012, **22**, 2327-2336.
- (24). K. Goushi and C. Adachi, *Appl. Phys. Lett.*, 2012, **101**, 023306.